On strain and damage interactions during tearing: 3D *in situ* measurements and simulations for a ductile alloy (AA2139-T3)

Thilo F. Morgeneyer[a,*], Thibault Taillandier-Thomas[a,b], Ante Buljac[a,b], Lukas Helfen[c,d], François Hild[b]

[a] *MINES ParisTech, PSL Research University, Centre des matériaux, CNRS UMR 7633, BP 87, F-91003 Evry, France*
[b] *LMT-Cachan, ENS Cachan/CNRS/Université Paris-Saclay, 61 avenue du Président Wilson, F-94235 Cachan Cedex, France*
[c] *ANKA/Institute for Photon Science and Synchrotron Radiation, Karlsruhe Institute of Technology (KIT), D-76131 Karlsruhe, Germany*
[d] *European Synchrotron Radiation Facility (ESRF), BP 220, F-38043 Grenoble cedex, France*

Abstract

Strain and damage interactions during tearing of a ductile Al-alloy with high work hardening are assessed *in situ* and in 3D combining two recently developed experimental techniques, namely, synchrotron laminography and digital volume correlation. Digital volume correlation consists of registering 3D laminography images. Via simultaneous assessments of 3D strain and damage at a distance of 1-mm ahead of a notch root of a thin Compact Tension-like specimen, it is found that parallel crossing slant strained bands are active from the beginning of loading in a region where the crack will be slanted. These bands have an intermittent activity but are stable in space. Even at late stages of deformation strained bands can stop their activity highlighting the importance of plasticity on the failure process rather than damage softening. One void is followed over the loading history and seen to grow and orient along the slant strained band at very late stages of deformation. Void growth and strain are quantified. Gurson-Tvergaard-Needleman-type simulations using damage nucleation for shear, which is based on the Lode parameter, are performed and capture

*Corresponding author, thilo.morgeneyer@ensmp.fr

slant fracture but not the initial strain fields and in particular the experimentally found slant bands. The band formation and strain distribution inside and outside the bands are discussed further using plane strain simulations accounting for plastic material heterogeneity in soft zones.

Keywords: A. Fracture mechanisms, A. Voids and inclusions, B. Metallic material, C. Finite elements, C. Mechanical testing

---

1. Introduction

The understanding and prediction of strain and damage interactions in ductile alloys remain a challenging topic due to the development of novel alloys and joining techniques, *e.g.,* for transport applications [1, 2]. This understanding is important for micromechanics-based development of new materials and the assessment of structural integrity.

The prediction of failure at various stress states still remains a challenge [3]. In particular, strain localization phenomena are important issues as they may reduce the toughness of structures [4]. Their prediction is difficult as the roles of plasticity and damage softening on localization need to be clarified [5]. Such strain localization phenomena in metals have been studied theoretically by Needleman and Tvergaard [6] who found that they are favored by material behaviors that form a sharp vertex on the yield surface, by material damage and by heating due to plastic deformation leading to thermal softening at high strain rates. The effect of softening in bands due to strain rate sensitivity has also been investigated [7]. Huang and Hutchinson assessed numerically the effect of voids and their distribution on strain localization in a band. Fleck *et al.* [8] analyzed theoretically the effect of nucleation and growth of voids in a shear band and showed that damage softening favors localization.

Another poorly understood phenomenon linked to localization is slant fracture during ductile tearing [9]. Slant fracture is hard to reproduce numerically [10]. This could be linked to numerical problems due to mesh dependence of local models [11]. Regularized models may overcome this issue but the reg-

ularization length then needs to be identified in an appropriate way. Slant fracture has successfully been simulated using shear void nucleation based on the Lode parameter [12] that actually resembles the shear modification of the Gurson model [13]. In Ref. [14] it has been shown via a computational cell simulation that the dissipated energy reaches a minimum when the crack is slanted. Experimentally, slant fracture is widely observed in thin walled structures [15] and can also lead to flip-flopping phenomena [16, 17] that are neither understood nor reproduced numerically.

Shear banding has also been attributed to Portevin-Le-Chatelier effect that leads to equally spaced rough bands on the surface of a Kahn tear test specimen made of Al-Li alloy [18]. In Ref. [19] the Coulomb fracture model and the Portevin-Le-Chatelier (PLC) model or dynamic strain aging (DSA) are formulated at the slip system scale and slant fracture could be reproduced.

In ductile damage modeling, where nucleation, growth and coalescence of voids is generally taken into account, efforts have been made to account for void shape effects. In particular, the changes of ellipsoidal voids have been accounted for in homogenization models [20]. It has been shown numerically that void reorientation can increase the susceptibility of the material to shear localization for triaxialities ranging between approximately 0.3 and 0.8 [21]. Void coalescence in combined tension and shear fields has been studied numerically in Ref. [22]. However, these models need to be validated via *in situ* experimental observations.

With the recent developments in 3D imaging techniques such as synchrotron tomography it has become possible to follow and quantify damage processes *in situ* at micrometer resolutions [23]. Even nondestructive observations at resolutions of tens of nanometers are now possible [24, 25]. *In situ* tomography is limited to axisymmetric (or stick-like) specimens with diameters of the order of 1 mm, which, in practice, may be relaxed by a factor of 3 to 5 if local tomography can be used [26]. In contrast, regions of interest in flat specimens can be imaged via synchrotron laminography [27, 28]. This technique has been applied to assess the underlying physical mechanisms of ductile crack initiation

and propagation [29, 30].

To evaluate 3D displacement fields in the bulk of imaged samples, two techniques are used, namely, feature tracking and volume correlation. The tracking technique consists of following the motion of particles or other features. It is performed either manually [31] or automatically [32, 33]. Digital volume correlation (DVC) provides either a cloud of 3D displacements for local-based registrations [34, 35, 36] or spatially continuous and dense displacement fields for global registrations [37, 38, 39]. For both techniques, additional markers have sometimes to be added to enable the tracking or registration procedure to be performed [40, 35, 41]. However, these additional markers may alter the deformation and degradation mechanisms. Even though the volume fraction of secondary features is very low in the alloy investigated in this study (*i.e.,* less than 1 % volume fraction) it was decided not to add any additional marker since they may become damage nucleation sites. In a feasibility analysis, it has been proven that global DVC could be used to measure 3D displacement fields even under such extreme conditions [42].

For an Al-Cu-Li alloy with low work hardening it has been shown with these techniques that slant strained bands precede the onset of damage and the slant crack [43]. This region of the sample has been shown to be in a plane strain state with respect to the crack propagation direction [44]. It has also been shown that the ratio between the strain in the band and outside of the band was of the order of 2 [43]. In other words the material outside the bands also deforms during every load step, except for the very last ones, but to a lesser extend than the material within the band. For the last load step deformation only occurs within the band. If the term "localization" refers to a state where plastic yielding takes place within the band and the outer region is plastically inactive, localization has only been measured at the very latest step. However, strain concentrations in a slant strained band were observed very early on and the scene for localization and fracture was already set. It is of interest for the understanding of strain and damage interactions if this way to deform is a general mechanism for these types of materials or only found in some particular

cases.

In this paper the interactions between strain, porosity and the final crack are assessed via DVC for laminography data already reported in Ref. [30], namely, for a ductile aluminum alloy containing pre-existing voids (AA2139 T3). After introducing the material and the experimental approach, the strain fields and their corresponding microstructure are investigated in a region 1-mm ahead of the notch root. Incremental and cumulated strain fields will be given. The response of one void in such a strain field is then assessed. The findings are compared with a Gurson-Tvergaard-Needleman-type model simulation using shear-based void nucleation in terms of strain fields. The strain distribution will be further discussed using 2D plane strain simulations that account for soft bands or randomly distributed soft zones.

2. Experimental configuration

2.1. Studied Material

The investigated material is an Al-Cu-Mg alloy (AA2139) in a naturally aged (*i.e.,* T3) condition. The material processing directions are the rolling direction (L), the transverse direction (T) and the short-transverse direction (S) in the through thickness direction. Figure 1(a) shows the grain size (mean value: 60 μm) in the L direction, in the T (mean value: 52 μm) and S (mean value: 24 μm) directions. These data have been obtained from optical microscopy on etched sections using a mean linear intercept method [45]. Figure 1(b) shows typical L-S and T-S sections of the material obtained by tomography. Intermetallic particles are seen in white and the aluminum matrix in gray. The intermetallic content has been determined to be 0.45 vol% and the initial void volume fraction 0.34 % [46]. The spacing of the particles and voids has been estimated using Feret dimensions of Voronoi cells around particles and pores. The spacing is in the order of 25 μm [46], which is an average upper bound.

The stress/strain curves in the L and T directions are shown in Figure 2 up to the ultimate tensile strength showing strong work hardening and high

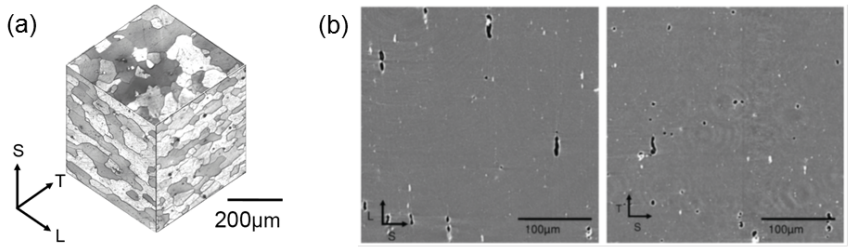

Figure 1: (a) Pseudo 3D cube showing the grain shapes (optical microscopy after etching). (b) 2D sections of reconstructed 3D synchrotron tomography data (after Ref. [45])

ductility (see Ref. [46] for mechanical properties and chemical composition). The material has a moderate texture and very limited anisotropy measured in stress-strain curves.

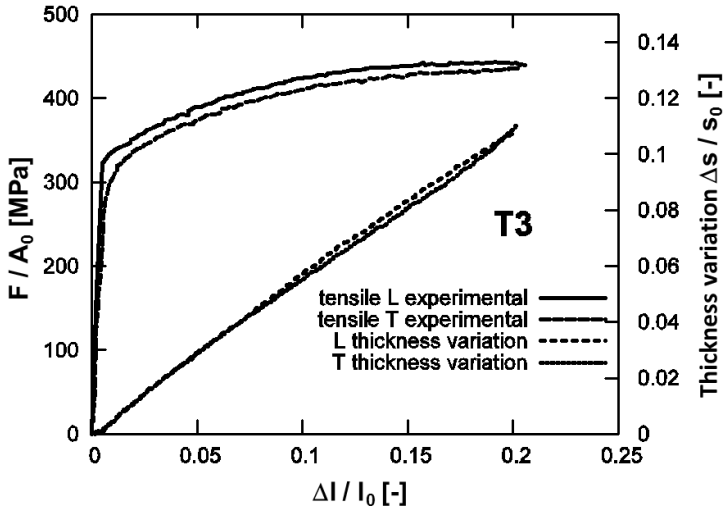

Figure 2: Engineering stress-strain curve for AA2139 T3 when loading in the L and T directions. The thickness variation is also given (after Ref. [46])

2.2. Laminography

Laminography imaging was performed on the instrument installed by the Karlsruhe Institute of Technology at the imaging beamline ID19 [47] of the European Synchrotron Radiation Facility (ESRF, Grenoble, France) in the conditions

described by Morgeneyer *et al.* [30, 42]. The main advantage of laminography compared to tomography is that large flat specimens can be used. Synchrotron laminography benefits from various contrast modes including propagation-based phase contrast used herein in addition to the conventional absorption employed in laboratory X-ray imaging. For large source-specimen distances, large sample environments (*e.g.,* mechanical testing devices) can be employed for high-resolution imaging without risk of collision during the scanning motion.

Similar to tomography, a series of digital radiographs is acquired while rotating the sample about the laminographic axis [47]. The latter is inclined with respect to the transmitted beam at an angle $0° < \theta < 90°$, see Figure 3. With the flat specimen oriented approximately perpendicular to the rotation axis, the average beam transmission can be optimized during the entire laminographic scan. Using filtered back-projection algorithms [48] different planes or complete 3D images with down to sub-micrometer resolution zoomed onto the large specimen can be reconstructed by a single scanning motion.

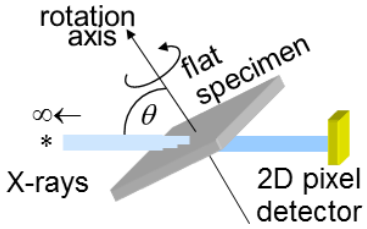

Figure 3: Schematic drawing of the laminography setup (after Ref. [42])

An inclination angle of the rotation axis of about 25° with respect to the beam normal was chosen as well as a monochromatic beam of 25 keV X-ray energy. Volumes were reconstructed from 1,500 angularly equidistant radiographs using a microscope-based indirect detector system with ×20 magnification [49] and an ESRF Frelon camera. The exposure time of each projection was 250 ms. The scanned region is ≈ 1 mm^3 in volume with a voxel size of 0.7 μm. This is where the flat-to-slant transition is typically observed [50]. The minimum specimen to detector distance is 70 mm leading to relatively strong edge enhancement

due to phase contrast. The resulting strongly contrasted edges facilitate the detection of voids and damage. For easier data handling, all 3D images consisting of 32-bit floating point values were converted into 8-bit gray level 3D images using the same linear dependence. As the same affine transformation is performed after reconstruction, the gray level distributions between the images are comparable. The final reconstructed volumes have a size of 2040 × 2040 × 2040 voxels. However, only the voxels where all projections contribute to the reconstruction exhibit all the directional information available, show similar noise statistics and therefore have been considered herein.

2.3. In situ mechanical experiment

To investigate strain and damage interactions *in situ*, a loading device was adapted to the environment given by the laminography scanning geometry (Figure 4(a)) [30]. In particular, the device was designed to present a low profile perpendicular to the sample plane, thereby avoiding obstruction of the beam during rotation. The screws (see Figure 4(b)) allow a stepwise crack mouth opening displacement (CMOD) to be prescribed [30]. Before each "load step," the region ahead of the notch was scanned by laminography. A load step consists of turning the 2 screws of the loading device leading to incremental openings of the notch, *i.e.,* a stepwise monotonic and quasi-static loading was applied.

The specimen (with dimensions 60 × 70 × 1 mm) contains a round notch with a radius of $R = 0.17$ mm and a 24-mm ligament (see Figure 4(b)). The loading configuration is T-L. Being close to standard tearing test geometries, this specimen provides relevant engineering conditions and allows for the development of plastic zones sizes as found in standard tests. The region ahead of the notch is loaded in tension and bending. A simple anti-buckling device (*i.e.,* flat plates) is used to limit out-of-plane displacements.

All the mechanical parameters are characterized as functions of the nominal CMOD obtained by the opening of the loading device in this study. The definitions of CMOD, crack length a are shown in Figure 4(b,d). The crack length is measured in the center of the 3D image/specimen and may, due to

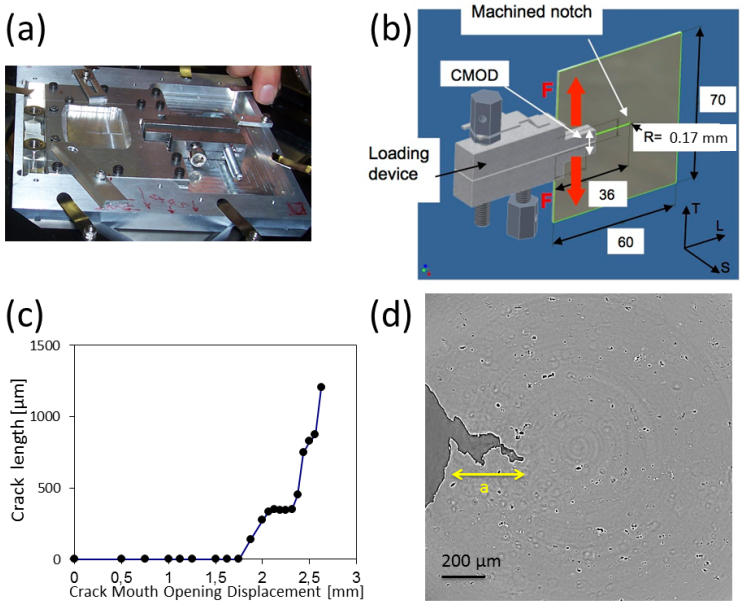

Figure 4: (a) Photograph of the specimen, loading device and anti-buckling frame mounted onto the laminography specimen holder; (b) drawing of the flat (1 mm) CT-like specimen and loading device; (c) measured crack length versus CMOD curve (every dot on the curve corresponds to one load increment and corresponding scan); (d) 2D section of reconstructed laminography data at mid thickness for load step CMOD = 2.125 mm

crack tunneling, be more accurate (and pessimistic) than traditional surface observations.

2.4. 3D kinematic measurements

The acquired scans can be used to measure 3D displacements fields by registering one gray level volume in the reference configuration f and a second volume g in the deformed configuration via DVC. Two different types of approaches can be followed. First local approaches consist of subdividing the region of interest (ROI) into a set of *independent* sub-volumes that are registered [34, 51, 35, 36]. An alternative approach is global so that the warping of the reference volume is analyzed globally and not locally [37]. One of the advantages of the latter approaches is that finite element kinematics can be considered thereby allowing

for regularized [52, 53] or integrated [54, 55] approaches.

In the following C8-DVC [37] will be considered. It consists of discretizing the volume of interest with 8-noded cubes (*i.e.,* C8 elements) whose edge length is denoted by ℓ. Trilinear displacement interpolations are used within each considered element. The DVC procedure consists of minimizing the global correlation residuals

$$\Phi_c = \sum_{\text{ROI}} \varphi^2(\mathbf{x}) \tag{1}$$

where

$$\varphi(\mathbf{x}) = |f(\mathbf{x}) - g(\mathbf{x} + \mathbf{u}(\mathbf{x}))| \tag{2}$$

with respect to the degrees of freedom associated with the parameterization of the displacement field $\mathbf{u}(\mathbf{x})$, where $\mathbf{x}$ denotes the location of all the voxels belonging to the ROI. The overall quality of the registration is measured by the global dimensionless residual

$$\rho_c = \frac{1}{\Delta f}\sqrt{\frac{\Phi_c}{|\text{ROI}|}} \tag{3}$$

where $\Delta f = \max_{\text{ROI}} f - min_{\text{ROI}} f$ denotes the dynamic range of the gray levels of the ROI in the reference configuration.

When a series of volumes in the deformed configuration is analyzed, two different strategies can be followed. First, when the strain levels remain lower than 10 %, the multiscale implementation [37] usually allows the whole series to be analyzed with f being the volume of the first scan [38]. Second, when larger strains occur, a first step of the analysis consists of evaluating the incremental displacement fields for which the deformed volume of the previous calculation becomes the reference volume of the next one. Once this first series of calculations is performed, it is possible to cumulate the displacements in a Lagrangian way.

For example, let us denote $\mathbf{u}_{01}(\mathbf{x}_0)$ the displacement field of scan 1 with respect to scan 0 expressed in the reference frame of scan 0. An incremental calculation between scan 1 and 2 will yield the displacement field $\mathbf{u}_{12}(\mathbf{x}_1)$ expressed in the frame of scan 1. To be cumulated, the incremental displacement

field $\mathbf{u}_{12}$ has to be evaluated for the location of $\mathbf{x}_0$ in the deformed configuration $\hat{\mathbf{x}}_1(\mathbf{x}_0) = \mathbf{x}_0 + \mathbf{u}_{01}(\mathbf{x}_0)$. Knowing the measured displacement field $\mathbf{u}_{12}(\mathbf{x}_1)$, it can be interpolated to be evaluated at $\hat{\mathbf{x}}_1$ by using the shape functions of the C8 discretization. Let $\hat{\mathbf{u}}_{12}$ denote this interpolated displacement field. The cumulated displacement field then reads

$$\mathbf{u}_{02}(\mathbf{x}_0) = \mathbf{u}_{01}(\mathbf{x}_0) + \hat{\mathbf{u}}_{12}(\mathbf{x}_0) \tag{4}$$

with

$$\hat{\mathbf{u}}_{12}(\mathbf{x}_0) = \mathbf{u}_{12}(\mathbf{x}_0 + \mathbf{u}_{01}(\mathbf{x}_0)) \tag{5}$$

In general, some of the nodal positions may require an extrapolation, namely, they lie outside the ROI in the reference configuration. In that case, among many options, two are implemented. If the aim is to stop the analysis at this stage, no extrapolation is required, they are considered as `NaN` (*i.e.,* not a number) and they are not visualized. Direct calculations may also be performed in which this first evaluation of the cumulated displacement field corresponds to the initial guess of a direct calculation from scan 0 to 2 [43]. In that case, the previous option cannot be used and extrapolated values should be assessed. The extrapolated value corresponds to the displacement of the closest node for which a measured estimate exists.

In the present DVC analyses, a volume of interest has been extracted from the scanned volume. Within this volume an initial ROI of $864 \times 608 \times 992$ voxels (*i.e.,* ≈ 600 μm $\times 425$ μm $\times 700$ μm) has been considered for correlation purposes and has been discretized with 32-voxel C8 elements. With such a discretization, $\approx 54,000$ kinematic degrees of freedom are measured. The choice of the element size in any DVC calculation results from a compromise between measurement uncertainty and spatial resolution [56, 42] (here twice the element size, *i.e.,* ≈ 45 μm). To evaluate the resolution of the measurement technique, two scans of the undeformed configuration were reconstructed when a small motion was prescribed between the two acquisitions. For 32-voxel ($\approx$ 22 μm) elements, the standard displacement resolution was found to be of the order of 0.2 voxel, and the corresponding standard equivalent strain resolution equal to 0.5 %.

These values are the largest levels below which the measurement cannot be distinguished from noise. From the loading state CMOD = 2.313 mm onward, the ROI was shifted away from the notch by 280 μm to avoid the damaged region and reach correlation convergence. In addition, a bigger ROI has been used (*i.e.,* $1248 \times 512 \times 992$ voxels) to be able to follow two voids in the microstructure in spite of large strain levels.

Based upon these results, the convergence criterion of the correlation calculations, which corresponds to the mean displacement increment between two consecutive iterations, is chosen to be equal to 10^{-4} voxel. It was checked that the mean correlation residual has reached a steady state for this criterion. The results are also checked by computing the correlation residuals voxel-wise, and their average value (*i.e.,* Φ_c or equivalently ρ_c). The mean and local residual levels are similar to those found by considering two subsequent acquisitions in which no deformation of the sample has occurred (*i.e.,* for the resolution analysis). Consequently, the reported results are deemed trustworthy.

The correlation analyses reported herein consist of estimating the total displacement field for each analyzed step with respect to the reference configuration up to loading step for which the CMOD is equal to 1.625 mm. From these Lagrangian measurements, the incremental displacement fields are directly given by the total displacement difference corresponding to two consecutive steps. The Green-Lagrange strain fields are estimated either with the total displacement fields, or with the incremental displacement fields. In both cases, the mean values per C8 element are reported. For the displacement field between the initial state and any load step for which the CMOD is greater than 1.5 mm the direct correlation could not yield a converged solution as strains are very high and damage nucleation started to set in. For this reason incremental correlations taking load state CMOD = 1.5 mm as a reference have been carried out. This procedure was also performed for the subsequent load steps.

3. Strain and damage interaction

3.1. Incremental fields

The objective of this work is to investigate the interactions between damage and strain during ductile tearing and, in particular, during the flat-to-slant crack transition. The challenge is to show both values simultaneously. Figure 5 highlights the way in which this simultaneous assessment of strain and damage is performed. A volume of interest has been extracted (Figure 5(a)). Its outer face is located 1080 μm ahead of the notch root and normal to the crack propagation direction. Figure 5(b) shows the 3D von Mises equivalent strain field in the ROI for a DVC analysis between the undeformed state (*i.e.,* CMOD = 0.0 mm) and when CMOD = 1.5 mm. In Figure 5(c) a new way to simultaneously show microstructure and strain fields is given. The strain field is made half transparent and it is laid over the underlying material microstructure as observed by laminography (*i.e.,* particles and porosity). The 2D slices (strain and microstructure) have been obtained at the *same* location in the investigated 3D volume. The underlying microstructure section shows the microstructure before loading as this is the reference state for the performed correlation.

This representation has been used for different load steps and *incremental* correlations in Figure 6. The underlying reference microstructure (at step n) is shown with an overlay of the *incremental* von Mises equivalent strain field for the correlation between steps n and $n+1$.

Figure 6(a) shows the strain field for a load increment starting from the unloaded state to load step CMOD = 1.5 mm. This is the largest direct correlation step that can be performed. Several intermediate steps were performed during the *in situ* experiment that will be shown in the sequel. When CMOD = 1.5 mm, there is no crack that has initiated from the initial notch. The von Mises equivalent strain field shows a heterogeneous distribution with an average level ≈ 10 %. Several parallel slant bands are observed at this relatively early stage of loading. Three bands oriented from the lower left part of the section to the upper right

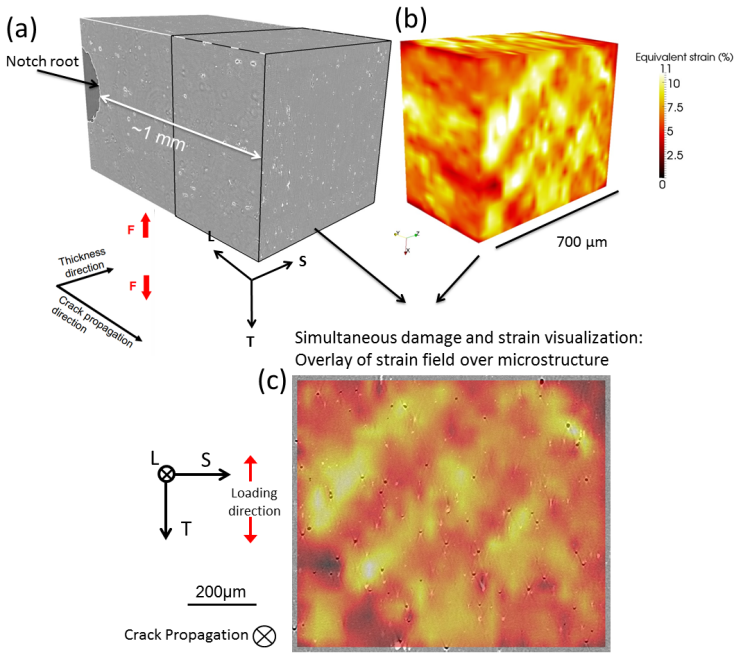

Figure 5: (a) 3D rendering of the initial microstructure and the ROI. (b) 3D rendering of the equivalent strain field in the extracted volume when CMOD = 1.5 mm. (c) 2D overlay of strain field over the initial microstructure

part seem to be prevalent. In this 2D section no clear link between the underlying voids and the strained bands is established. The magnitude of the strain in the bands is about twice as high (*i.e.*, 13 %) as in the material between the bands. This ratio has already been found for an aluminum alloy with less work hardening and initial porosity [43]. However, the latter material mainly showed one localized band and not several parallel bands as seen here. In addition, the slant strained band was less diffuse than in the present case. On this 2D section two particular voids of the underlying microstructure are encircled. They are also highlighted for the following load increments. This representation allows the spatial location of the strained bands to be assessed with respect to their underlying microstructure and if these bands "stick" to the microstructure.

In Figure 6(b) an overlay of the incremental strain field between CMOD = 1.5 mm and CMOD = 2.0 mm is shown over the underlying microstructure of the load

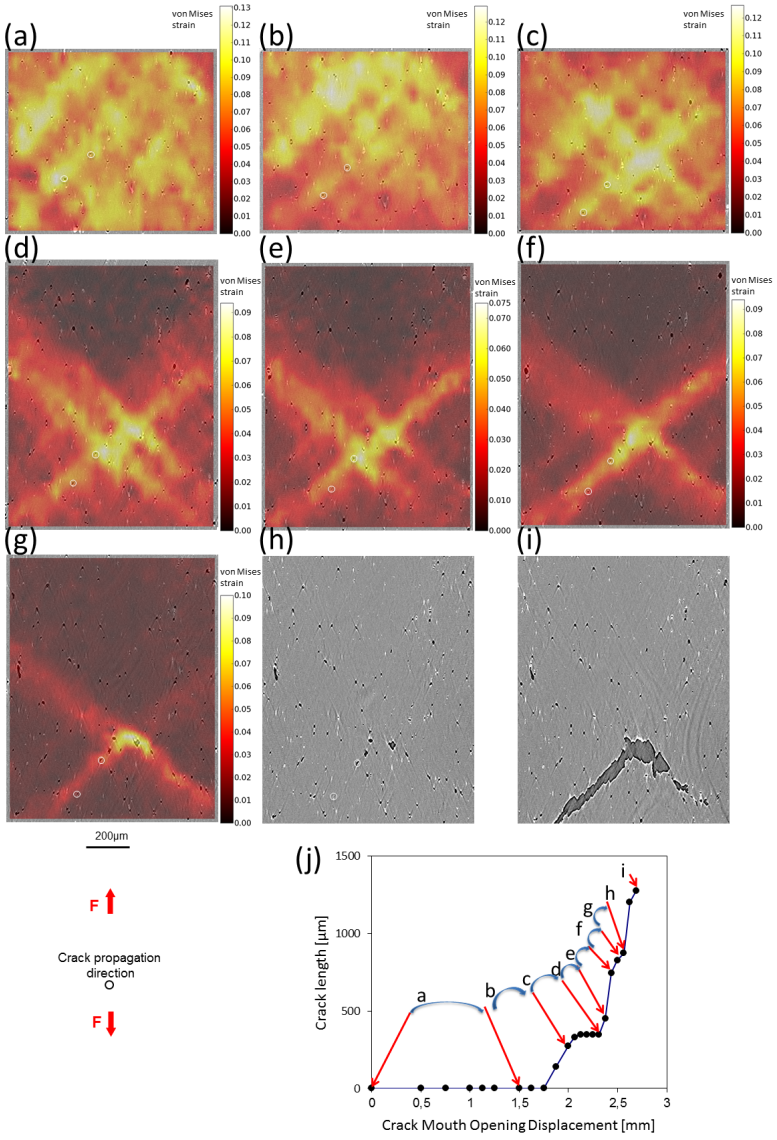

Figure 6: Overlay of *incremental* equivalent strain fields (half transparent) over the microstructure 1080 μm ahead of the notch root. (a)-(g) 2D sections of laminography data and equivalent strain fields. The microstructure is shown in state n for incremental correlations between n and $n+i$. Two reference voids are encircled in white on the microstructure for every load step; (h),(i) microstructure showing damage and the final crack path; (j) load steps corresponding to the shown sections

step corresponding to CMOD = 1.5 mm. Out of the three slant strained bands that were active in the first load step the upper one is the most active. The other two bands are less active. Compared to Figure 6(a) the strained band has shifted downward, but this is only due to a shift of the entire region of interest compared to an arbitrarily chosen reference point. The comparison of the strained bands with respect to the underlying microstructure shows that the band is motionless in the material coordinate system, namely, the same voids and particles are found within the band. The void and particle evolution seems very limited (*i.e.,* void nucleation, growth or shape change are not striking at this scale of observation). It should however be noted that at this loading stage there is already a crack propagating from the notch root (*i.e.,* outside the ROI investigated herein), which may influence the strain fields.

The following load increment, from CMOD = 2.0 mm to CMOD = 2.313 mm, generates an activity of the two upper strained bands (Figure 6(c)). The lower band of the two is again located above the two encircled voids as for the first step (Figure 6(a)). However, in this step there is another very active band oriented normal to the two previous bands. Even more slant crossing bands are active in the center of the specimen. They form a 45-degree tilted square divided into 4 smaller squares yielding an inclined "waffle-like" pattern that shows characteristic distances between the strained bands of the order of $150 - 250$ μm. No noticeable void and particle growth is seen for this load step.

For the next load increment the extracted volume has been increased symmetrically in the loading direction in order to be able to still follow the two voids encircled in the previous sections. A small incremental step from CMOD = 2.313 mm to CMOD = 2.375 mm is shown. The small remote load increment leads to high local strains as the crack approaches this region. From the lower left part of this region to the upper right part only one strained band is active (Figure 6(d)). It is still located above the two encircled voids. Normal to this band two other parallel strained bands are active. The strain field is now substantially more localized than in Figure 6(c). A very similar strain pattern is seen for the next load step from CMOD = 2.375 mm to CMOD = 2.438 mm (Figure 6(e)). There

is still very little damage to be seen in the microstructure at this location and, if any, it is rather diffuse and also located in regions that do not belong to any strained band.

In Figure 6(f) the same strained band from the lower left to the upper right corner of the image is mainly active. Only one out of the two bands normal to this one, *i.e.,* the upper band, is now active. The latter is particularly active in the lower part of the investigated region. It is noteworthy that at these late stages of loading there is still not only a single strained band active but a competition between several bands that have undergone tens of percents of strain. The next load step from CMOD = 2.438 mm to CMOD = 2.5 mm is the last one for which a trustworthy correlation could be achieved (Figure 6(g)), namely, the residuals were still very close to those observed when two undeformed volumes are registered. It can be seen for the underlying microstructure that a notable damage evolution now sets in. In the region where the strained bands cross, voids grow. The upper one of the two encircled voids shows a reorientation that has already been reported [50] for the same experiment. With the present work the corresponding strain fields for the void shape changes are known.

Figure 6(h) shows the microstructure of load step CMOD = 2.5 mm without the corresponding strain field. Voids in the region where the two strained bands cross grow further. This highlights that in this area the main assumption for trustworthy DVC, which is the conservation of gray levels is no longer satisfied as damage sets in. However, the measured strain concentration where the two strained bands cross is plausible, as, in addition, void growth is seen here that is surely a result of highly localized strain activity. The lower half of the strained bands is more active than the upper half. In Figure 6(i) the final crack path is observed (*i.e.,* CMOD = 2.625 mm). A roof top crack is seen, which has not fractured the full section yet. The crack has followed the second slant strained band that is present from the very early loading onward. The two voids that had been encircled in the previous load increments now contribute to the final fracture surface.

In summary, several slant, crossing and parallel strained bands with inter-

mittent activity were found. Failure occurred along one band that was already active since the very beginning of the loading history.

3.2. Cumulated fields

In this section some cumulated strain fields are assessed for very large load intervals from the unloaded state. This is only possible via numerically cumulating the incremental displacement fields as explained above. Due to the large strains direct correlations are no longer possible. Accumulation of the fields is only possible up to CMOD = 2.313 mm as after this step the 3D ROI has been shifted away from the notch to avoid damaged areas for correlation purposes. For the cumulated displacement fields the equivalent strain fields are then derived and shown in Figure 7. In the lower parts of Figures 7(b-c) the information on the displacement is no longer available. This is due to the fact that the ROI size was kept constant for all correlations and that the material elongated along the loading direction.

The striking finding in Figure 7(b) compared to Figure 7(a) is that the strained bands do not move in space. The band in the upper left corner is the most active, which is consistent with the fact that the strain field shown in Figure 6(b) was "added." The maximum equivalent strain in this slice is now increased to ≈ 0.24. In Figure 7(c) a cumulated field is shown corresponding to strains between load step CMOD = 0.0 mm and CMOD = 2.313 mm. The equivalent strained band pattern is still similar to the previous ones but the maximum magnitude has now increased to ≈ 0.33. The bands do not move in space and, as a consequence, do not even out the strain distribution but keep a concentrated pattern made up of several bands. This is surprising as the regions between the strained bands could be expected to be softer than the bands and easier to deform if a uniform material behavior is assumed. Local variability in stress/strain behavior could be at the origin of such behavior. Damage evolution is not striking until this loading state and thus should not be of prior importance to softening.

The strain profile along a line perpendicular to the strained bands is shown

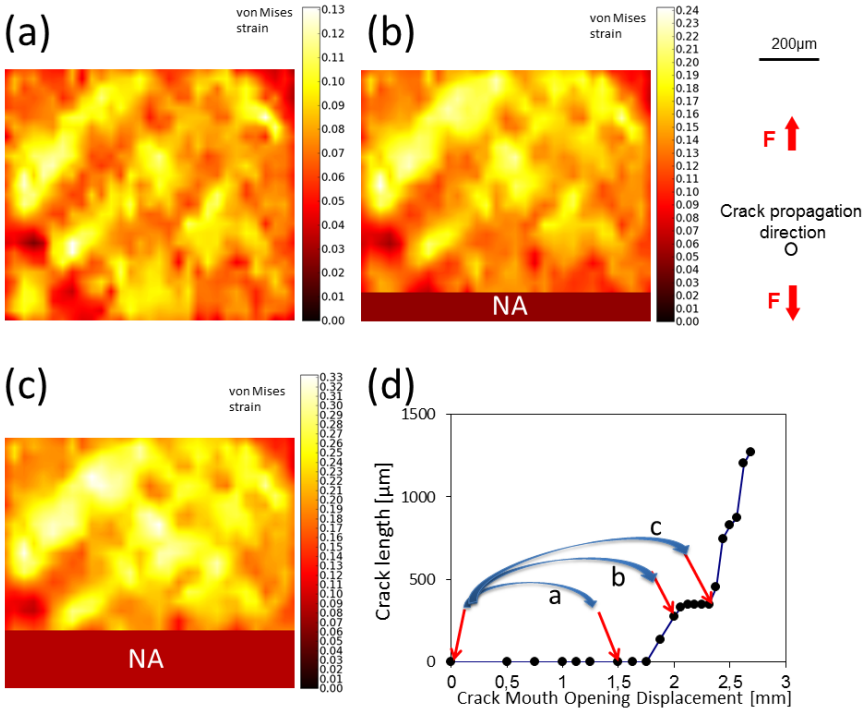

Figure 7: 2D sections of *cumulated* equivalent von Mises strain fields. (a) Direct correlation from CMOD = 0.0 mm to CMOD = 1.5 mm. (b) One cumulation from CMOD = 0.0 mm to CMOD = 2.0 mm. (c) Two cumulations from CMOD = 0.0 mm to CMOD = 2.313 mm (the coordinate system is shown in its initial state)

in Figure 8. This graph confirms the spatial stability of the strained bands. The ratio of the equivalent strain in the main bands over the strain outside the bands lies between 1.5 and 2. For the band that will lead to the final failure this ratio is somewhat lower. This result is comparable to the strain ratio that was reported for AA 2198 T8 [43]. The main difference is that several bands are active in the present case.

3.3. Small load increments from the initial state

In this section strain fields for small steps are reported when DVC is performed from the unloaded step (CMOD = 0.0 mm) to the load step before crack initiation (*i.e.,* CMOD = 1.5 mm). The incremental strain fields in this load

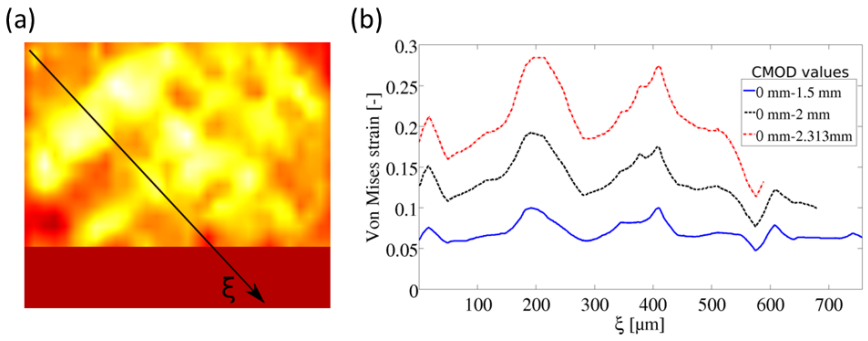

Figure 8: (a) 2D section of cumulated fields (equivalent von Mises strain) with indication of the location for the strain profile. (b) Strain profile for the direct and cumulated strain fields from CMOD = 0.0 mm to CMOD = 2.313 mm

interval from the unloaded state are also given. The latter investigation is made in order to interpret the incremental strain activity (Δp_{eq}) as could also be done in an FE simulation that accounts for instabilities.

Figure 9(a) shows the strain field obtained for the first load step carried out during the *in situ* test (*i.e.,* CMOD = 0.5 mm). In this step a maximum equivalent strain of 0.03 is obtained. However, the three strained bands from the lower left corner of the image to the upper right corner can already be seen. These bands remain visible for a substantially larger load increment (Figure 6(a)). Damage nucleation or growth is negligible at this step of loading. A similar result was also found for AA2198 T8 [43]. The strained bands found herein are less localized.

Figure 9(b) shows the strain field for a correlation from the initial unloaded state to the second load step (*i.e.,* CMOD = 0.75 mm). The strain field has a similar pattern as the first one, but the strain magnitude increases up to 0.05. For the subsequent load steps (Figures 9 (c-f)) the same observation holds. It should be noted that the last strain field (see Figure 9(f)) is the same as that shown in Figure 6(a). This result indicates that the characteristic strain pattern hardly evolves over the loading history, which is also consistent with the very large strain measurements shown in Figure 7.

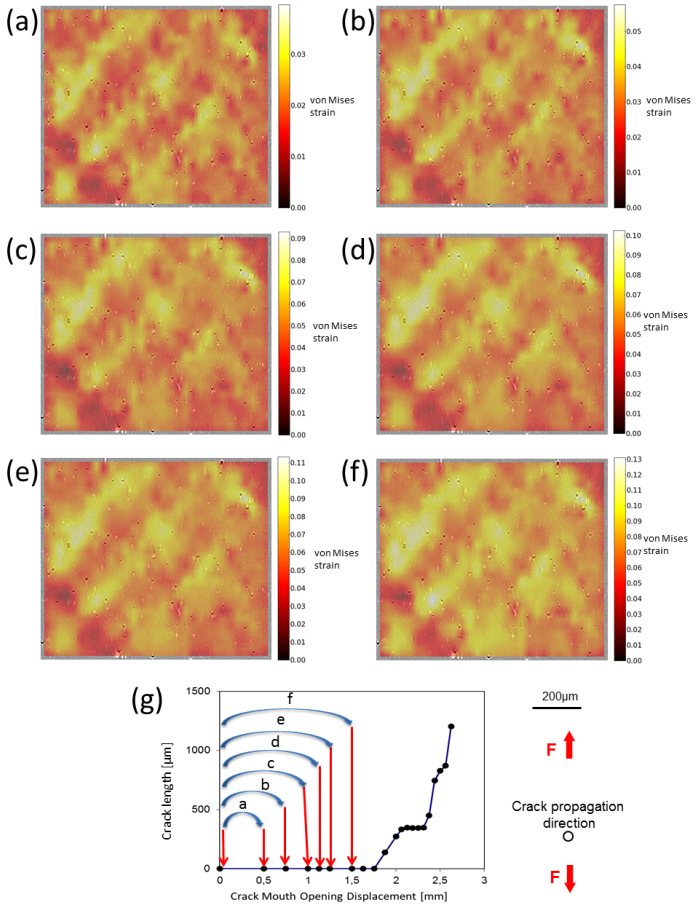

Figure 9: 2D section of 3D laminography and DVC data. Overlay of the smallest possible direct equivalent strain fields (half transparent) over the microstructure in its initial state

Incremental strain fields are shown in Figure 10 in the undeformed coordinate system of the initial material microstructure. Figure 10(a) shows the same strain field as Figure 6(a). The subsequent strain fields, in contrast, have an intermittent activity. In Figure 10(b) the next incremental strain field is reported. The noisy nature of the field is due to a lower signal to noise ratio of the measurements (*i.e.,* the maximum strain is about 0.02). The three strained bands can still be guessed. In the subsequent load step the upper strained bands seem more active than the lower ones. The next three incremental fields appear

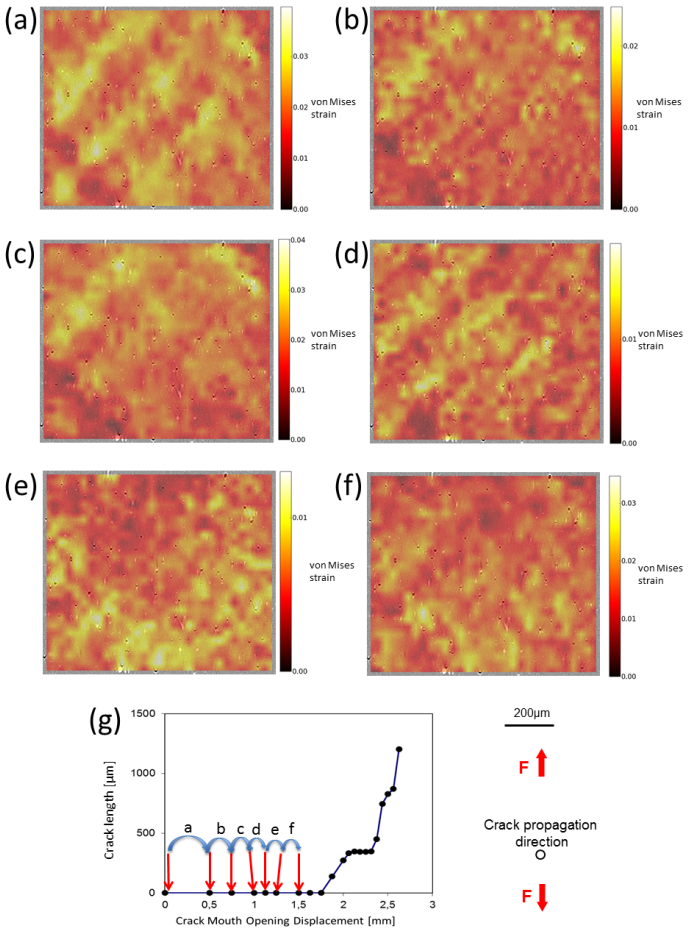

Figure 10: 2D section of 3D laminography and DVC data. Overlay of the smallest possible incremental equivalent strain fields (half transparent) over the microstructure in its initial state

noisy due to the low maximum strain level (as low as 0.02 for Figure 10(d)). However, the strain activity is higher in the lower part of the field.

In Figure 11, incremental strain fields in the same loading interval (CMOD = 0.0 mm to CMOD = 1.5 mm) are also given. However, bigger load increments are assessed in the correlation (n to $n + 2$) to obtain a higher signal to noise ratio. Figure 11(a) corresponds to Figure 9(b). The three strained bands are visible. Figure 9(b) shows the incremental strain field from load step CMOD = 0.75 mm

to CMOD = 1.125 mm. A similar strain pattern as in the initial step is observed. The strain activity is somewhat higher in the upper part of the region. In Figure 11(c) the largest strain activity is seen in the lower part of the 2D section. This activity may be consistent with Portevin Le Chatelier (PLC)-like behavior spreading the strain in an even manner. However, the characteristic strain pattern always remains, *i.e.,* most of the strain activity takes place in the strained bands and not in the surrounding strain "valleys."

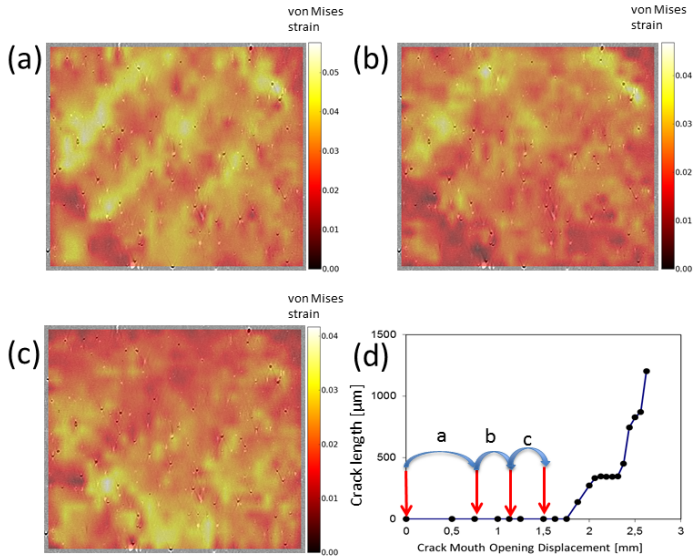

Figure 11: 2D section of 3D laminography and DVC data. Overlay of *incremental* equivalent strain fields n to $n+2$ (half transparent) over microstructure (the microstructure in its initial state)

In Figure 12 the strain field for incremental steps from CMOD = 0.0 to CMOD = 1.0 mm (Figure 12(a)) and from CMOD = 1.0 mm to CMOD = 1.5 mm (Figure 12(b)) are reported. The three strained bands are again observed in Figure 12(a). In Figure 12(b) it can be seen that the strain activity is more pronounced in the lower part of the 2D section. This behavior has already been seen in Figure 11(c) and might be attributed to PLC-like effects.

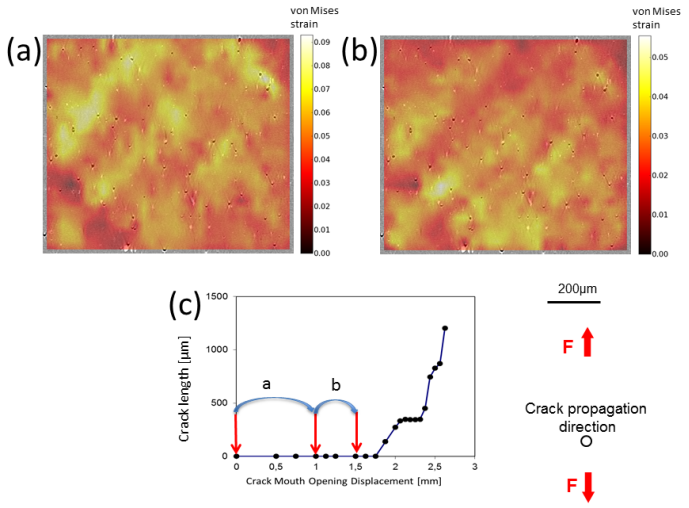

Figure 12: 2D section of 3D laminography and DVC data. Overlay of incremental equivalent strain fields n to $n+3$ (half transparent) over the microstructure in the initial state

3.4. Void shape evolution in strained bands

In previous sections the existence of intermittent strained bands has been shown. In this section the interest lies on the evolution of a pre-existing void (*i.e.,* hydrogen micropore [57]) up to fracture in such a strained band. The void is located 45 μm farther away from the notch than the 2D section shown in the previous figures. It is situated at about mid-thickness of the specimen (see Figures 13(a-b) [50]). This void was located in the final strained band that led to fracture as illustrated by the overlay of the strain field over the underlying microstructure (Figure 13(b)). It undergoes substantial growth only at late stages of deformation. From Figure 7(c) it is known that the corresponding equivalent strain is of the order of 0.30 in this region, but growth is moderate as seen in Figure 13(e).

In the subsequent load steps the void grows in the loading direction and turns toward the orientation of the strained band. During the next load steps, void growth mainly occurs along the strained band direction. This is consistent with a local mode I and III loading state [9] that lets the void grow in a mixture of tensile and simple shear fields [21]. This void reorientation has been shown

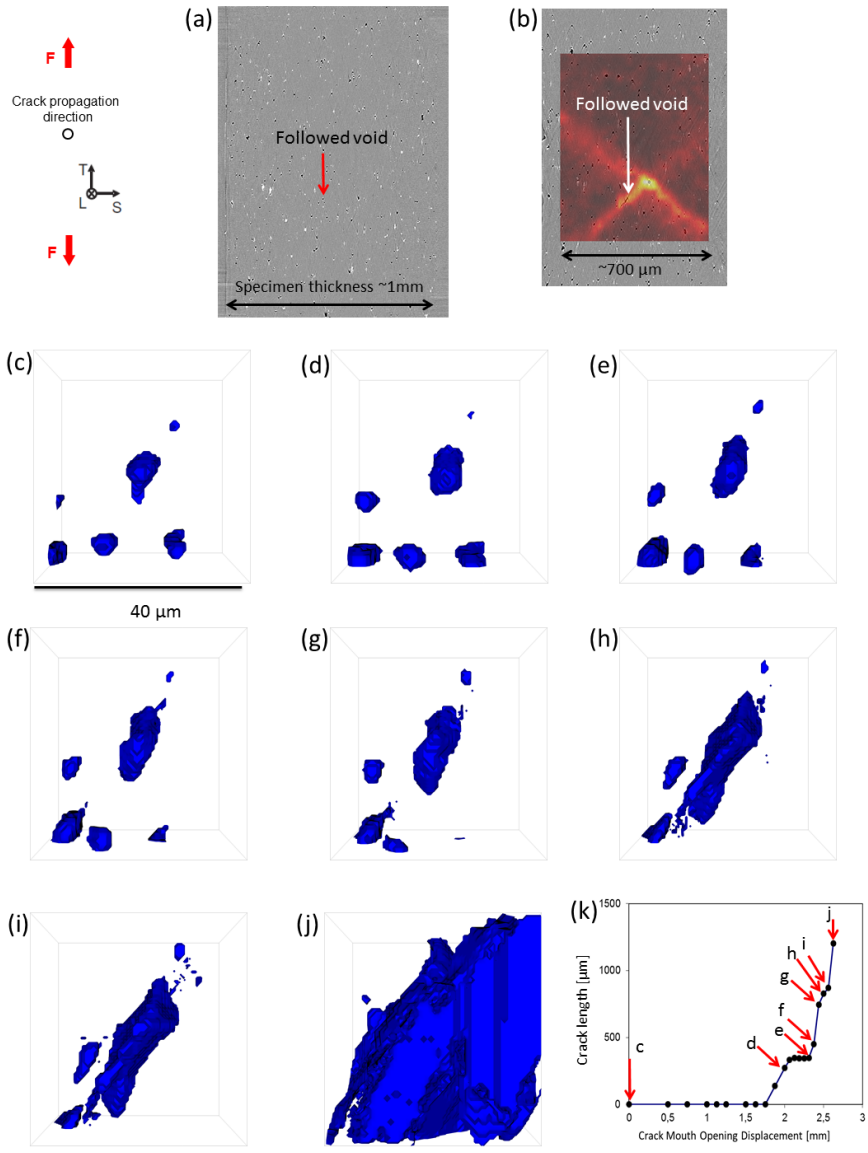

Figure 13: 3D void visualization of reconstructed laminography data. (a) Through-thickness section with location of the void 1125 μm from the notch. (b) Overlay of strain field for step CMOD = 2.5 mm to CMOD = 2.563 mm over microstructure at CMOD = 2.5 mm. (c)-(j) Void growth. (k) Indication of the corresponding load step

numerically to facilitate localization phenomena. In the final stages smaller damage features become visible that are consistent with void nucleation and growth on a second population of particles at high levels of strain. However, very narrow crack regions are also seen in Figure 13(i), which are consistent with the void sheeting phenomenon. This void fully contributes to the final crack.

The void growth versus local equivalent von Mises strain has been further quantified in Figure 14. This figure confirms that despite the fact that the

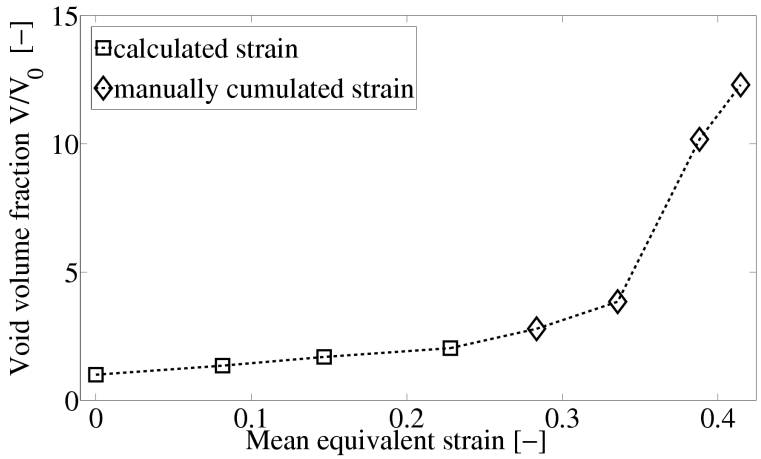

Figure 14: Void volume fraction for one void (see Figure 13) versus measured von Mises equivalent strain.

strain profiles are already heterogeneous from early loading stages onward no substantial void growth occurs until elevated levels of strain (more than 0.30 in the present case). This is also in agreement with results obtained by unit cell calculations [46]. They predict for a stress triaxiality of 1.25 a void volume (vv) of 3 times the initial volume at about 0.15-0.35 strain. However, void coalescence is predicted in unit cell calculations at higher void volume fraction level than in the experiment (about 12 times the initial vv) and also at higher strain (0.3-0.5). In the experimental data void growth acceleration occurs at 0.3 strain and for a vv that is 3 times higher than the initial one, *i.e.,* substantially earlier than in the unit cell calculations. The complex strain field encountered

herein, which may lead to mixed tensile and shear states, may be at the origin of this behavior [21]. It is worth noting that only one void has been studied. An investigation considering more voids would be useful to gain a better statistical representation of these processes.

4. Simulations

To interpret these experimental results, and in particular the slant strained band formation at early loading stages, simulations are carried out. In Ref. [50] Gurson-Tvergaard-Needleman-type simulations consistent with the experimentally observed crack growth have been carried out for the present material and sample geometry. These simulations did not show inclined bands in the strain fields nor slant fracture. A shear-based void nucleation term is used [12], which had yielded slant fracture, to compare the initial measured and predicted strain fields and final fracture.

4.1. 3D Gurson-Tvergaard-Needleman-type simulations

The modification for void nucleation under shear [12] is briefly recalled. The idea is to use the Lode parameter of the strain rate tensor to detect if the material deforms under a shear strain state and nucleate voids in that case. The Lode parameter for the strain rate tensor assuming incompressibility reads

$$\dot{\pi} = \frac{3\dot{p}_2}{\dot{p}_1 - \dot{p}_3} \text{ with } \dot{p}_1 \geq \dot{p}_2 \geq \dot{p}_3 \tag{6}$$

where $\dot{p}_i$ are the eigen values of the plastic strain rate tensor. Using the Lode parameter of the strain rate tensor, the shear-controlled nucleation rate is then expressed as

$$\dot{f_n} = A_n \dot{p} \tag{7}$$

with

$$A_n = A_2^{shear} \exp\left[-\left(\frac{\dot{\pi}}{\dot{\pi}_0}\right)^2\right] \quad \text{when} \quad p \geq p_{crit}^{shear} \tag{8}$$

where $\dot{\pi}_0$ is an adjustable parameter of the Gaussian function. For the rest of the Gurson-Tvergaard-Needleman-type model the reader is referred to Refs. [46, 12]. The model parameters are given in Table 1.

Table 1: Material parameters for the laws used herein

Behavior								
Elastoplastic	E (GPa)	ν	$R_0(MPa)$	K_0	K_1	k_1	K_2	k_2
	70	0.3	250	0.054	1.12	7.15	0.273	187
Damage	q_1	q_2	f_0	f_c	A_n^1	A_n^{shear}	p_c^{shear}	$\dot{\pi}_0$
	1.97	0.91	0.33 % avg.	4.5 %	0.05	2.0	0.1	0.033

The results of the simulations with the new term for void nucleation are shown in Figure 15. The strain fields are given in the same ROI as the measured fields. For some increments the strain magnitude is different from the experiment. It can be seen that the initial simulated strain fields do not resemble the measured ones. The simulated strain fields resemble those of von Mises-type plasticity simulations or classical Gurson-Tvergaard-Needleman-type simulation [43] with a characteristic circular strain pattern. This is expected as the shear nucleation terms only sets in after a critical strain of 0.10. Only at late stages do the strain fields begin to be slanted. In contrast to the experimental findings only one band is active and not several parallel strain bands with intermittent activity. The slant fracture and flat-to-slant crack transition are successfully reproduced in this simulation. The fact that the initial strain fields are not found by the simulation indicates that the plasticity model needs to be modified to enhance the predictions.

4.2. Effect of material heterogeneity

4.2.1. Soft slant bands

The measurements of the strain fields ahead of the notch show parallel strained bands that are stable in space but have intermittent activity. The ratio of the strains within the bands and outside is of the order of 1.5-2.0 (see

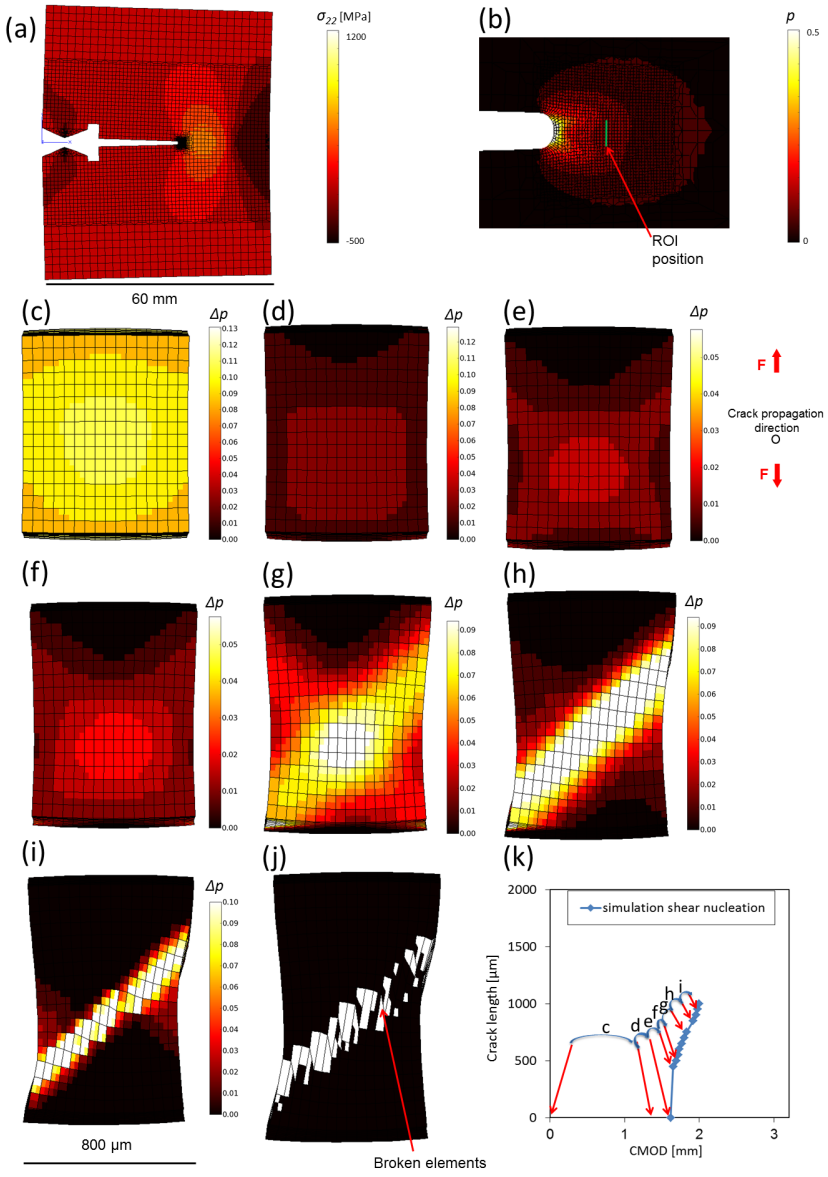

Figure 15: Results of a 3D simulation of the CT-like specimen using a Gurson-Tvergaard-Needleman model combined with a shear void nucleation term. (a) Stress field in the loading direction. (b) Equivalent strain field in the plastic zone. (c)-(i) incremental strain fields in the ROI for load steps corresponding to Figure 6 1050 μm ahead from the notch root. (j) Final crack position. (k) Indication of the corresponding load step

Figure 8). To interpret further the existence of these bands and in particular the strain distribution 2D simulations are performed to account for material heterogeneity [58]. The simulations are carried out in plane strain conditions as it has been shown that crack propagation occurs under such conditions. Isotropic hardening is described by

$$R(p) = R_0 \left[1 + K_0 p + K_1 \left(1 - e^{-k_1 p}\right) + K_2 \left(1 - e^{-k_2 p}\right)\right] \tag{9}$$

where the material parameters R_0, K_0, K_1, k_1, K_2, k_2 are given in Table 1. The weakening is described by multiplying the hardening law with a perturbation factor $0 < x < 1$

$$R(p) = (1 - x) R_0 \left[1 + K_0 p + K_1 \left(1 - e^{-k_1 p}\right) + K_2 \left(1 - e^{-k_2 p}\right)\right] \tag{10}$$

The mesh with the soft zone and the line along which the strain profile is analyzed are given in Figure 16(a). Loading of the upper and lower ends of

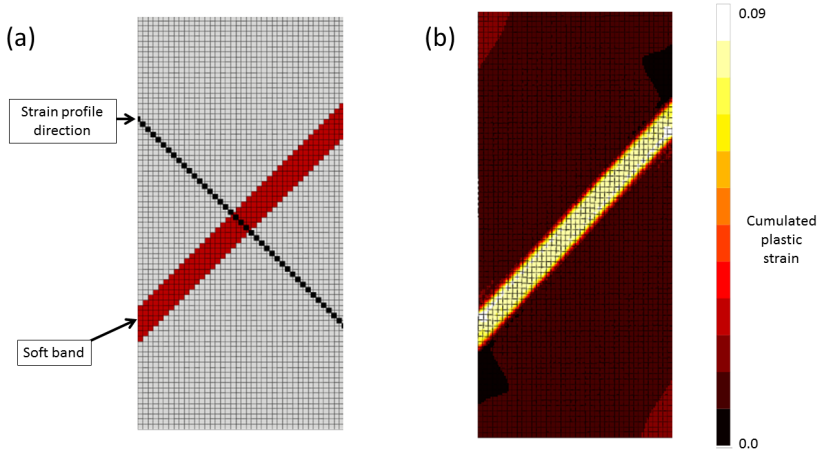

Figure 16: 2D plane strain simulation using a slant soft band. (a) 2D mesh. (b) Equivalent plastic strain field when $x = 10$ %

the meshed zone leads to a slant strain distribution for a perturbation of 10 % shown in Figure 16(b).

The strain profiles normal to the meshed soft band are reported in Figure 17. The equivalent plastic strain increases in both regions (*i.e.,* within and outside

the band). The strain ratio is of the order of 2 for a perturbation $x = 10$ %.

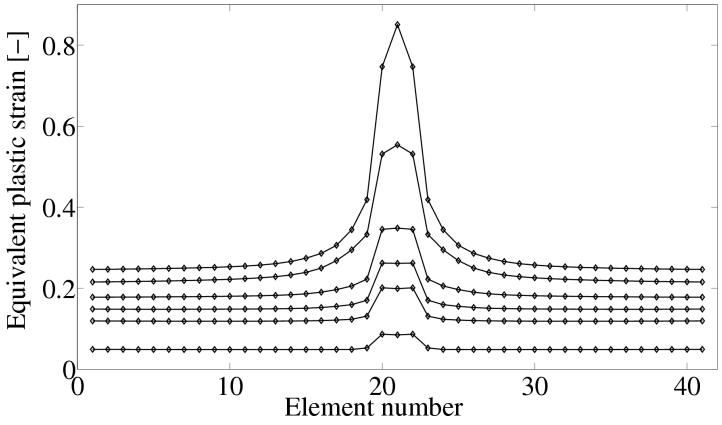

Figure 17: Equivalent strain profiles normal to the band (see Figure 16(a)) for a 10-% perturbation

Figure 18 shows the change of the strain ratio for different perturbation levels. The stronger the perturbation the higher the initial strain ratio and the earlier the final increase of the strain ratio. In the experimental case the strain ratio is still of the order of 2 for a strain outside the band of ≈ 0.22. A soft perturbation of the order of 10 % reproduces rather well these experimental findings.

4.2.2. Randomly distributed soft zones

There is no evident reason for soft zones in the material to be distributed in slant bands. Consequently soft zones with a size of 50 μm$\times$50 μm are randomly distributed in an additional simulation. These dimensions are close to the mean grain size of the studied aluminum alloy. The soft zones were randomly distributed in the central part of the meshed region. The soft phase fraction has been chosen to be the same as in the previously reported calculation with a soft slant band. The soft zone distribution is depicted in Figure 19(a). The resulting equivalent strain field is shown in Figure 19(b). Some development of slant bands occurs at 0.14 average equivalent strain, which is relatively early

in comparison with the experimental evidence reported herein. The ratio between the bands and the surrounding material is less (*i.e.,* ≈ 1.15) than for the simulation where all soft zones are located in a single slant band.

4.3. Discussion

Combining three dimensional *in situ* imaging of a flat specimen with DVC it is shown that slant strained bands precede the development of damage in the slant fracture region. These parallel slant bands have an intermittent activity. The crossing bands initially form a "waffle"-like pattern due to strain ridges and valleys. The ratio of the strain within the bands and the surrounding material is of the order of 1.5 to 2.

Three-dimensional FE simulations using von Mises plasticity or a Gurson-Tvergaard-Needleman-type model do not capture the slant bands. With a standard Gurson-Tvergaard-Needleman-model the crack remains flat. The flat-to-slant crack transition can be reproduced successfully using a Lode parameter-based void nucleation term in a Gurson-Tvergaard-Needleman-model. The early slant bands are, however, not reproduced.

The strain partitioning is further investigated via plane strain simulations where a slant soft zone is modeled. A plane strain condition had been identified for the crack propagation direction in the region where the crack is slanted [44]. For a perturbation of 10%, strain partitioning between the band and the surrounding material, and a strain level at localization are in agreement with the experimental findings. A softening effect is thus identified rather than shear localization where all strains would localize within the band.

The question that arises is what could be at the origin of these bands. The heterogeneous strain fields could be linked to heterogeneous microstructures and resulting plasticity [58]. Local material heterogeneity caused by crystallographic texture, which is referred to as roping, could also be a possibility [59]. In that case these local textures are the result of ex-super grains that existed at some point during material processing. However, the characteristic lengths identified in Ref. [59] are substantially larger than what is found herein, namely, more

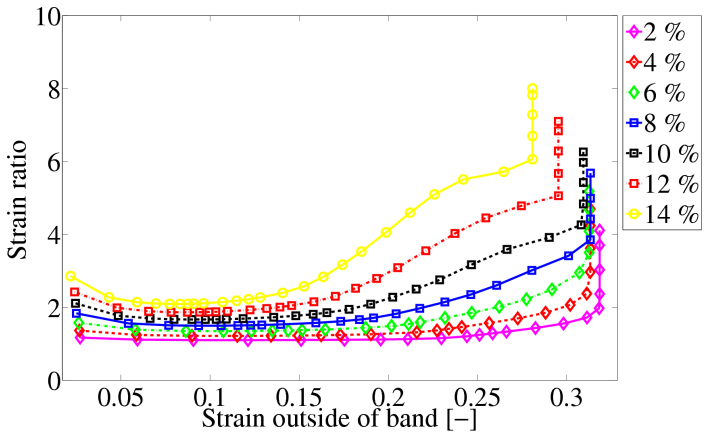

Figure 18: Strain ratio versus strain outside the band for different perturbation levels (2 % $\leq$ $x \leq$ 14 %)

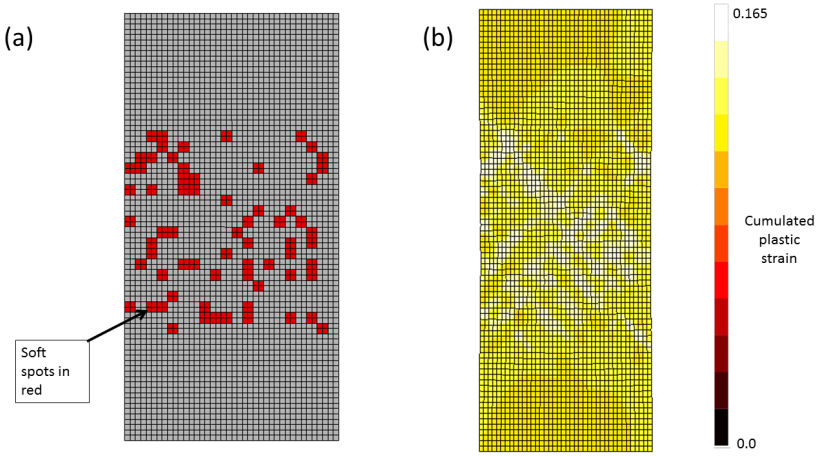

Figure 19: 2D plane strain simulation using randomly distributed soft zones. (a) 2D mesh. (b) Equivalent plastic strain field when the mean level is equal to 0.14 and $x = 10$ %

than 1 mm [59] compared to about 200 μm herein. In addition, the bands that are found are slanted and evenly spaced. There is no obvious reason to find such slant grain arrangements in soft zones. Additionally the characteristic spacing, ordered nature and intermittent activity of the bands makes a purely material heterogeneity based origin less likely.

Using a mesh with randomly distributed soft zones to model soft grain distribution, slant bands are obtained at early loading stages under plane strain conditions. These soft zones may be a possible origin of the phenomena reported herein. However, the strain ratio within and outside the bands is not similar to the experimental findings. Using different surface fractions or softness, results might be obtained that could be closer to the experimental findings. However, the intermittent activity of the bands is not captured through these effects.

In the present models no ingredients to reproduce the intermittent strained band activity are used. Origins of the intermittent nature of the strained bands could be DSA (*i.e.,* Portevin-Le-Chatelier effect [60, 19]). This observation is also supported by the fact that even at very late stages of deformation strained bands may become inactive and damage softening does not seem to influence these processes on the first order. It is, however, surprising that the experimentally measured strained bands are stable in space with respect to microstructural features. This is generally not found for moving PLC bands on smooth specimens as in these cases the strained bands move in time and even out the strain heterogeneities in the different regions. Here, however, the notch naturally concentrates the strain fields and may prevent the bands from moving. Similar strained bands have been found on Kahn tear test sample surfaces made of Al-Li alloy [18] after tearing. Deformation patterns in slant crossing bands ahead of notches have also been suggested in early works on these phenomena [61].

Further, it is experimentally shown that inside the strained bands voids change shape and rotate to align along the direction of the band. The question arises whether the shape evolution of pre-existing voids can lead to strain localization and damage softening. It is noteworthy that this evolution takes place only at the latest stages of deformation. It is thus more likely that this

void growth is the result of previous, and thus governing, deformation and concentration in strained bands. It is certainly of interest to investigate the effect of void shape changes in such strained bands on the fracture resistance of the material. It is likely that there will be an additional localization effect due to void rotations [21].

The problem in modeling slant fracture remains the mesh dependence of the simulations [11]. The slant fracture found herein was reproduced by a shear void nucleation term based on the Lode parameter [12]. However, the mesh dependence is still an issue. In addition, several slant bands could not be reproduced. To create bands with intermittent activity a PLC-type model may be used [19] but mesh dependence and computation times are also problematic for such types of models.

Experiments on other types of Al alloys and specimen geometries should also be performed to confirm the presence of slant bands and PLC effects. Nonlocal models are needed to get more reliable predictions of localized phenomena but the regularization length is still to be physically understood and identified. The present finding could also add another length to the commonly used particle or void spacing, which is the strained band spacing.

5. Conclusions

Damage and strain interactions have been assessed *in situ* and within the material bulk during ductile tearing. The region of interest is located 1080 μm ahead of a notched 1-mm thick plate made of ductile aluminum alloy containing initial porosities ($\approx$ 0.33 vol%) and particles ($\approx$ 0.45 vol%). This analysis is made possible by the combination of *in situ* synchrotron laminography and digital volume correlation using the material microstructure contrast. The overlay of strain and microstructure maps has yielded the following results:

- Several parallel, crossing and slant strained bands are active from the very early stages of loading (*i.e.,* max. 0.03 equivalent von Mises strain).

- The analysis of incremental strain fields shows that the activity of the bands is intermittent over the whole loading history.

- The spatial location of these bands compared to the microstructure is stable, *i.e.,* the strain activity is not evening out the strain fields.

- Even very concentrated (strained) bands with high von Mises equivalent strain levels (*i.e.,* 0.10) may become inactive and other bands become active at very late stages of loading.

- The typical strained band spacing is $150 - 250$ μm.

- The ratio of the equivalent strain within and outside the bands is about 1.5 to 2.

- In the local area of observation substantial void growth could not be detected at micrometer resolution before the occurrence of strained bands.

- The fact that strained bands may switch off at the end of the test indicates that the mechanisms at play for strain concentration may differ from damage softening.

- The observed slant strained bands at early loading stages cannot be reproduced using a Gurson-Tvergaard-Needleman-type model with Lode parameter-based shear void nucleation. The flat to slant crack transition is however successfully reproduced.

- 2D plane strain simulations accounting for a soft zone yield strain ratios within the band and the surrounding material similar to the measurements for a 10-% weakening. A softening effect is thus identified rather than shear localization where all strains would localize within the band. Using randomly distributed soft zones, slant strained bands can be obtained. The ratio of the strain within and outside the bands is, however, substantially lower than in the experimental findings.

Last, investigations on other Al-alloys and specimen geometries would be useful to confirm the present results, which have also be found on a low work hardening alloy (*i.e.,* AA2198 T8 [43]).

Acknowledgements

The financial support by Fédération Francilienne de Mécanique and Agence Nationale de la Recherche (ANR-14-CE07-0034-02 grant for COMINSIDE project) are gratefully acknowledged. Constellium C-Tec is acknowledged for material supply. The authors would also like to acknowledge ESRF for providing beamtime (experiment MA1006), Dr. M. Mavrogordato and Prof. I. Sinclair for help with the experiment. They particularly thank Prof. J.W. Hutchinson for discussing strain partitioning.

References

[1] T. Le Jolu, T. F. Morgeneyer, A. Denquin, M. Sennour, A. Laurent, J. Besson, A.-F. Gourgues-Lorenzon, Microstructural characterization of internal welding defects and their effect on the plastic behavior of FSW joints of AA2198 Al-Cu-Li alloy, Metall. Mat. Trans. A 45 (2014) 5531–5544.

[2] T. Le Jolu, T. F. Morgeneyer, A. Denquin, A.-F. Gourgues-Lorenzon, Fatigue lifetime and tearing resistance of AA2198 alloy friction stir welds: Effect of defects, Int. J. Fat. 70 (2015) 463–472.

[3] J. Papasidero, V. Doquet, D. Mohr, Determination of the Effect of Stress State on the Onset of Ductile Fracture Through Tension-Torsion Experiments, Exp. Mech. 54 (2) (2014) 137–151.

[4] J. Rice, The Localization of Plastic Deformations, North-Holland, 1976, pp. 207–220.

[5] C. Tekoğlu, J. W. Hutchinson, T. Pardoen, On localization and void coalescence as a precursor to ductile fracture, Phil. Trans. Royal Soc. London A373 (2038) (2015) 20140121.

[6] A. Needleman, V. Tvergaard, Analyses of Plastic Flow Localization in Metals, Appl. Mech. Rev. 45 (3S) (1992) S3–S18.

[7] A. Needleman, The Effect of Rate Dependence on Localization of Deformation and Failure in Softening Solids, J. Appl. Mech. 82 (2) (2015) 021002–7.

[8] N. Fleck, J. Hutchinson, A phenomelogical theory for strain gradient effects in plasticity, J. Mech. Phys. Solids 41 (12) (1993) 1825–1857.

[9] E. Mahgoub, X. Deng, M. Sutton, Three dimensional stress and deformation fields around flat and slant cracks under remote mode I loading conditions, Eng. Fract. Mech. 70 (2003) 2527–2542.

[10] J. Besson, Continuum models of ductile fracture: A review, Int. J. Damage Mech. 19 (2010) 3–52.

[11] J. Besson, D. Steglich, W. Brocks, Modeling of crack growth in round bars and plane strain specimens, Int. J. Solids Struct. 38 (46-47) (2001) 8259–8284.

[12] T. F. Morgeneyer, J. Besson, Flat to slant ductile fracture transition: Tomography examination and simulations using shear-controlled void nucleation, Scripta Mat. 65 (2011) 1002–1005.

[13] K. Nahshon, J. Hutchinson, Modification of the gurson model for shear failure, Eur. J. Mech. A/Solids 27 (2008) 1–17.

[14] J. Besson, C. McCowan, E. Drexler, Modeling flat to slant fracture transition using the computational cell methodology, Eng. Fract. Mech. 104 (2013) 80–95.

[15] T. Pardoen, F. Hachez, B. Marchioni, P. Blyth, A. Atkins, Mode I fracture of sheet metal, J. Mech. Phys. Solids 52 (2004) 423–452.

[16] S. El-Naaman, K. Nielsen, Observations on mode I ductile tearing in sheet metals, Eur. J. Mech. A/Solids 42 (2013) 54–62.

[17] B. Simonsen, R. Tornqvist, Experimental and numerical modelling of ductile crack propagation in large-scale shell structures, Marine Struct. 17 (1) (2004) 1–27.

[18] D. Delafosse, G. Lapasset, K. LP, Dynamic strain-aging and crack propagation in the 2091 Al-Li alloy, Scripta Metall. Mat. 29 (11) (1993) 1379–1384.

[19] G. Rousselier, S. Quilici, Combining porous plasticity with Coulomb and Portevin-Le Chatelier models for ductile fracture analyses, Int. J. Plasticity 69 (2015) 118–133.

[20] T.-S. Cao, M. Maziere, K. Danas, J. Besson, A model for ductile damage prediction at low stress triaxialities incorporating void shape change and void rotation, Int. J. Solids Struct. 63 (2015) 240–263.

[21] D. Song, M. Agoras, P. P. Castaneda, The evolution of pore shape and orientation in plastically deforming metals: Implications for macroscopic response and shear localization, Mech. Mat. 90 (2015) 47–68.

[22] M. E. Torki, A. A. Benzerga, J. B. Leblond, On Void Coalescence Under Combined Tension and Shear, J. Appl. Mech. 82 (7, SI).

[23] E. Maire, P. J. Withers, Quantitative X-ray tomography, Int. Mat. Rev. 59 (1) (2014) 1–43.

[24] T. Morgeneyer, H. Proudhon, P. Cloetens, W. Ludwig, Q. Roirand, L. Laiarinandrasana, E. Maire, Nanovoid morphology and distribution in deformed HDPE studied by magnified synchrotron radiation holotomography, Polymer 55 (2014) 6439–6443.

[25] E. Nizery, H. Proudhon, J. Buffiere, P. Cloetens, T. F. Morgeneyer, S. Forest, Three dimensional characterization of intermetallic particles in high-strength aluminium alloys using synchrotron X-ray tomography, Phil. Mag. 95 (25) (2015) 2731–2746.

[26] L. Laiarinandrasana, T. F. Morgeneyer, H. Proudhon, F. N'guyen, E. Maire, Effect of multiaxial stress state on morphology and spatial distribution of voids in deformed semi-crystalline polymer assessed by X-ray tomography, Macromolecules 45 (2012) 4658–4668.

[27] L. Helfen, T. Baumbach, P. Mikulík, D. Kiel, P. Pernot, P. Cloetens, J. Baruchel, High-resolution three-dimensional imaging of flat objects by synchrotron-radiation computed laminography, Appl. Phys. Lett. 86 (7) (2005) 071915.

[28] L. Helfen, A. Myagotin, P. Mikulík, P. Pernot, A. Voropaev, M. Elyyan, M. Di Michiel, J. Baruchel, T. Baumbach, On the implementation of computed laminography using synchrotron radiation, Rev. Sci. Instrum. 82 (063702).

[29] Y. Shen, T. F. Morgeneyer, J. Garnier, L. Allais, L. Helfen, J. Crepin, Three-dimensional quantitative in-situ study of crack initiation and propagation in AA6061 Al-alloy sheets via synchrotron laminography and finite-element simulations, Acta Mat. 61 (2013) 2571–2582.

[30] T. F. Morgeneyer, L. Helfen, I. Sinclair, H. Proudhon, F. Xu, T. Baumbach, Ductile crack initiation and propagation assessed via in situ synchrotron radiation computed laminography, Scripta Mat. 65 (2011) 1010–1013.

[31] H. Toda, I. Sinclair, J. Buffière, E. Maire, T. Connolley, M. Joyce, K. H. Khor, P. Gregson, Assessment of the fatigue crack closure phenomenon in damage-tolerant aluminium alloy by in-situ high-resolution synchrotron X-ray microtomography, Phil. Mag. 83 (21) (2003) 2429–2448.

[32] H. Toda, I. Sinclair, J. Buffière, E. Maire, K. Khor, P. Gregson, T. Kobayashi, A 3D measurement procedure for internal local crack driving forces via synchrotron X-ray microtomography, Acta Mat. 52 (2004) 1305–1317.

[33] M. Kobayashi, H. Toda, Y. Kawai, T. Ohgaki, K. Uesugi, D. Wilkinson, T. Kobayashi, Y. Aoki, M. Nakazawa, High-density three-dimensional mapping of internal strain by tracking microstructural features, Acta Mat. 56 (2008) 2167–2181.

[34] B. Bay, T. Smith, D. Fyhrie, M. Saad, Digital volume correlation: three-dimensional strain mapping using X-ray tomography, Exp. Mech. 39 (1999) 217–226.

[35] M. Bornert, J. Chaix, P. Doumalin, J. Dupré, T. Fournel, D. Jeulin, E. Maire, M. Moreaud, H. Moulinec, Mesure tridimensionnelle de champs cinématiques par imagerie volumique pour l'analyse des matériaux et des structures, Inst. Mes. Métrol. 4 (2004) 43–88.

[36] E. Verhulp, B. van Rietbergen, R. Huiskes, A three-dimensional digital image correlation technique for strain measurements in microstructures, J. Biomech. 37 (9) (2004) 1313–1320.

[37] S. Roux, F. Hild, P. Viot, D. Bernard, Three dimensional image correlation from X-Ray computed tomography of solid foam, Comp. Part A 39 (8) (2008) 1253–1265.

[38] F. Hild, E. Maire, S. Roux, J. Witz, Three dimensional analysis of a compression test on stone wool, Acta Mat. 57 (2009) 3310–3320.

[39] J. Réthoré, N. Limodin, J. Buffière, F. Hild, W. Ludwig, S. Roux, Digital volume correlation analyses of synchrotron tomographic images, J. Strain Analysis 46 (2011) 683–695.

[40] S. Nielsen, H. Poulsen, F. Beckmann, C. Thorning, J. Wert, Measurements of plastic displacement gradient components in three dimensions using marker particles and synchrotron X-ray absorption microtomography, Acta Mat. 51 (8) (2003) 2407–2415.

[41] K. Haldrup, S. Nielsen, J. Wert, A General Methodology for Full-Field Plastic Strain Measurements Using X-ray Absorption Tomography and Internal Markers, Exp. Mech. 48 (2008) 199–211.

[42] T. F. Morgeneyer, L. Helfen, H. Mubarak, F. Hild, 3D digital volume correlation of synchrotron radiation laminography images of ductile crack initiation: An initial feasibility study, Exp. Mech. 53 (2013) 543–556.

[43] T. F. Morgeneyer, T. Taillandier-Thomas, L. Helfen, T. Baumbach, I. Sinclair, S. Roux, F. Hild, In situ 3D observation of early strain localisation during failure of thin Al alloy (2198) sheet, Acta Mat. 69 (2014) 78–91.

[44] A. Buljac, T. Taillandier-Thomas, T. F. Morgeneyer, L. Helfen, S. Roux, F. Hild, Slant strained band development during flat to slant crack transition in AA 2198 T8 sheet: in situ 3D measurements, Int. J. Fract. (DOI: 10.1007/s10704-015-0052-z).

[45] T. F. Morgeneyer, M. Starink, I. Sinclair, Evolution of voids during ductile crack propagation in an Al-alloy sheet toughness test studied by micro-computed tomography, Acta Mat. 56 (2008) 1671–1679.

[46] T. F. Morgeneyer, J. Besson, H. Proudhon, M. Starink, I. Sinclair, Experimental and numerical analysis of toughness anisotropy in AA2139 Al-alloy sheet, Acta Mat. 57 (2009) 3902–3915.

[47] T. Weitkamp, P. Tafforeau, E. Boller, P. Cloetens, J. P. Valade, P. Bernard, F. Peyrin, W. Ludwig, L. Helfen, J. Baruchel, Parallel-beam imaging at the ESRF beamline ID19: current status and plans for the future, Vol. 1234 of Proceedings SRI 2009, AIP Conference Proceedings, 2010, pp. 83–86.

[48] A. Myagotin, A. Voropaev, L. Helfen, D. Hanschke, T. Baumbach, Efficient volume reconstruction for parallel-beam computed laminography by filtered backprojection on multi-core clusters., IEEE Transactions on Image Processing 22 (12) (2013) 5348–5361.

[49] P.-A. Douissard, A. Cecilia, X. Rochet, X. Chapel, T. Martin, T. van de Kamp, L. Helfen, T. Baumbach, L. Luquot, X. Xiao, J. Meinhardt, A. Rack, A versatile indirect detector design for hard X-ray microimaging, J. Instrum. 7 (2012) P09016.

[50] T. Ueda, L. Helfen, T. F. Morgeneyer, In-situ laminography study of three-dimensional individual void shape evolution at crack initiation and comparison with GTN-type simulations, Acta Mat. 78C (2014) 254–270.

[51] T. Smith, B. Bay, M. Rashid, Digital volume correlation including rotational degrees of freedom during minimization, Exp. Mech. 42 (3) (2002) 272–278.

[52] H. Leclerc, J. Périé, S. Roux, F. Hild, Voxel-scale digital volume correlation, Exp. Mech. 51 (4) (2011) 479–490.

[53] T. Taillandier-Thomas, S. Roux, T. F. Morgeneyer, F. Hild, Localized strain field measurement on laminography data with mechanical regularization, Nucl. Instr. Meth. Phys. Res. Sect. B 324 (2014) 70–79.

[54] A. Bouterf, S. Roux, F. Hild, J. Adrien, E. Maire, Digital volume correlation applied to X-ray tomography images from spherical indentation tests on lightweight gypsum, Strain 50 (5) (2014) 444–453.

[55] F. Hild, A. Bouterf, L. Chamoin, F. Mathieu, J. Neggers, F. Pled, Z. Tomičević, S. Roux, Toward 4d mechanical correlation, Adv. Mech. Simul. Eng. Sci. 3 (DOI:10.1186/s40323-016-0070-z) (2016) 1–26.

[56] H. Leclerc, J. Périé, F. Hild, S. Roux, Digital volume correlation: What are the limits to the spatial resolution?, Mech. & Indust. 13 (2012) 361–371.

[57] H. Toda, H. Oogo, K. Uesugi, M. Kobayashi, Roles of Pre-Existing Hydrogen Micropores on Ductile Fracture, Mat. Trans. 50 (9) (2009) 2285–2290.

[58] J. Hutchinson, V. Tvergaard, Shear band formation in plane-strain, Int. J. Solids Struct. 17 (5) (1981) 451–470.

[59] L. Qin, M. Seefeldt, P. V. Houtte, Analysis of roping of aluminum sheet materials based on the meso-scale moving window approach, Acta Mat. 84 (2015) 215–228.

[60] H. Wang, C. Berdin, M. Maziere, S. Forest, C. Prioul, A. Parrot, P. Le-Delliou, Portevin-Le Chatelier (PLC) instabilities and slant fracture in C-Mn steel round tensile specimens, Scripta Mat. 64 (5) (2011) 430–433.

[61] G. Hahn, A. Rosenfield, Local yielding and extension of a crack under plane stress, Acta Metall. 13 (3) (1965) 293–306.